



# **Multispecies Reacting Flow Model for the Plasma Efflux of an ETC Igniter—Application to an Open-Air Plasma Jet Impinging on an Instrumented Probe**

**by Michael J. Nusca, William R. Anderson, and Michael J. McQuaid**

**ARL-TR-3227**

**July 2004**

## **NOTICES**

### **Disclaimers**

The findings in this report are not to be construed as an official Department of the Army position unless so designated by other authorized documents.

Citation of manufacturer's or trade names does not constitute an official endorsement or approval of the use thereof.

Destroy this report when it is no longer needed. Do not return it to the originator.

# **Army Research Laboratory**

Aberdeen Proving Ground, MD 21005-5066

---

---

**ARL-TR-3227**

**July 2004**

---

## **Multispecies Reacting Flow Model for the Plasma Efflux of an ETC Igniter—Application to an Open-Air Plasma Jet Impinging on an Instrumented Probe**

**by Michael J. Nusca, William R. Anderson, and Michael J. McQuaid  
Weapons and Materials Research Directorate, ARL**

REPORT DOCUMENTATION PAGE			Form Approved OMB No. 0704-0188	
Public reporting burden for this collection of information is estimated to average 1 hour per response, including the time for reviewing instructions, searching existing data sources, gathering and maintaining the data needed, and completing and reviewing the collection information. Send comments regarding this burden estimate or any other aspect of this collection of information, including suggestions for reducing the burden, to Department of Defense, Washington Headquarters Services, Directorate for Information Operations and Reports (0704-0188), 1215 Jefferson Davis Highway, Suite 1204, Arlington, VA 22202-4302. Respondents should be aware that notwithstanding any other provision of law, no person shall be subject to any penalty for failing to comply with a collection of information if it does not display a currently valid OMB control number. <b>PLEASE DO NOT RETURN YOUR FORM TO THE ABOVE ADDRESS.</b>				
1. REPORT DATE (DD-MM-YYYY) July 2004		2. REPORT TYPE Final		3. DATES COVERED (From - To) January 1997–December 2000
4. TITLE AND SUBTITLE Multispecies Reacting Flow Model for the Plasma Efflux of an ETC Igniter— Application to an Open-Air Plasma Jet Impinging on an Instrumented Probe			5a. CONTRACT NUMBER	
			5b. GRANT NUMBER	
			5c. PROGRAM ELEMENT NUMBER	
6. AUTHOR(S) Michael J. Nusca, William R. Anderson, and Michael J. McQuaid			5d. PROJECT NUMBER 6122618H8000	
			5e. TASK NUMBER	
			5f. WORK UNIT NUMBER	
7. PERFORMING ORGANIZATION NAME(S) AND ADDRESS(ES) U.S. Army Research Laboratory ATTN: AMSRD-ARL-WM-BD Aberdeen Proving Ground, MD 21005-5066			8. PERFORMING ORGANIZATION REPORT NUMBER ARL-TR-3227	
9. SPONSORING/MONITORING AGENCY NAME(S) AND ADDRESS(ES)			10. SPONSOR/MONITOR'S ACRONYM(S)	
			11. SPONSOR/MONITOR'S REPORT NUMBER(S)	
12. DISTRIBUTION/AVAILABILITY STATEMENT Approved for public release; distribution is unlimited.				
13. SUPPLEMENTARY NOTES				
14. ABSTRACT The U.S. Army Research Laboratory (ARL) is investigating the electrothermal-chemical (ETC) gun concept. As part of this program, ARL has recently begun a comprehensive study on the interaction of the plasma efflux from an ETC igniter with solid propellant grains. The goal of this work is to elucidate the relevant physical, mechanical, and chemical mechanisms that underlie the observed ballistic effects in ETC guns that can lead to useful performance gains once an understanding of these mechanisms is achieved. This report describes the first phase of the modeling effort in support of this plasma-propellant interaction project. A time-accurate computational fluid dynamics code was used that included high-temperature thermodynamics, variable specific heats and transport properties (viscosity and thermal conductivity), and finite-rate (nonequilibrium) chemical kinetics. Validation of this code used a series of experiments with an ETC igniter fired into open air, generating an unsteady flowfield in which a measurement probe is placed. Computer simulations revealed important gas dynamic and chemical details of the plasma jet as it interacted with the probe and represented the first such detailed modeling of ETC plasma efflux.				
15. SUBJECT TERMS gun charges, solid propellant, multiphase flow, computer simulation				
16. SECURITY CLASSIFICATION OF:			17. LIMITATION OF ABSTRACT  UL	18. NUMBER OF PAGES  30
a. REPORT UNCLASSIFIED	b. ABSTRACT UNCLASSIFIED	c. THIS PAGE UNCLASSIFIED		
				19b. TELEPHONE NUMBER (Include area code) 410-278-6108

---

## Contents

---

<b>List of Figures</b>	<b>iv</b>
<b>List of Tables</b>	<b>iv</b>
<b>Acknowledgments</b>	<b>v</b>
<b>1. Introduction</b>	<b>1</b>
<b>2. Description of Open-Air Plasma Jet Experiment</b>	<b>2</b>
<b>3. Previous Modeling Efforts</b>	<b>7</b>
<b>4. Multispecies Reacting Flow CFD Code</b>	<b>7</b>
<b>5. Results and Discussion</b>	<b>10</b>
<b>6. Conclusions</b>	<b>16</b>
<b>7. References</b>	<b>17</b>
<b>Distribution List</b>	<b>20</b>

---

## List of Figures

---

Figure 1. ETC gun concept. ....	1
Figure 2. Schematic of plasma generator and pressure probe also showing computational domain.....	3
Figure 3. Current and power histories.....	4
Figure 4. Efflux density and velocity histories. ....	4
Figure 5. Efflux pressure and temperature histories. ....	5
Figure 6. Efflux species histories.....	5
Figure 7. Schematic of gas dynamic features in a highly underexpanded jet.....	10
Figure 8. Computed Mach number contours. ....	12
Figure 9. Measured and computed pressure at the probe tip. ....	13
Figure 10. Computational results displayed in eight contour variables for 0.13 ms. ....	14
Figure 11. Computational results displayed in eight contour variables for 0.22 ms. ....	15

---

## List of Tables

---

Table 1. Species concentrations (moles/m <sup>3</sup> ) at 0.22 ms and four locations along the centerline.....	6
---	---

---

## **Acknowledgments**

---

The Plasma-Propellant Interaction Workunit, headed by Dr. Richard Beyer, at the U.S. Army Research Laboratory (ARL) funded this project. The Department of Defense Major Shared Resources Centers supplied supercomputer time at ARL and the Naval Oceanographic Office.

INTENTIONALLY LEFT BLANK.



---

## 1. Introduction

---

Future military engagements will require weapons systems exhibiting longer range and greater accuracy. One of the technologies under investigation to achieve these goals is the electrothermal-chemical (ETC) propulsion concept, shown schematically in figure 1. In the ETC gun, energy which is stored either in batteries or in a rotating device is converted on demand into an electrically generated plasma (resulting from the ablation of polyethylene material in a capillary), which is then injected into the chamber in a howitzer or gun. This plasma energy is used to ignite the chemical propulsion charge (e.g., solid propellant) as well as enhance gun performance by taking advantage of a number of unique plasma characteristics. For example, a low-density plasma jet can more efficiently ignite charges of high loading density (HLD), can control propellant mass-generation rates ( $\dot{m}$ ), can reduce propellant charge temperature sensitivity (i.e., the variation of gun performance with changing ambient temperature [2, 3]) and can shorten ignition delay (i.e., the time interval between firing of the igniter and ignition of the propellant [4]). Plasma igniters also eliminate the conventional chemical igniter and can thus enhance the safety aspects of the overall gun propulsion system. All of these observations have a significant effect on the ballistics of ETC gun systems and can lead to a useful improvement in gun performance and accuracy.

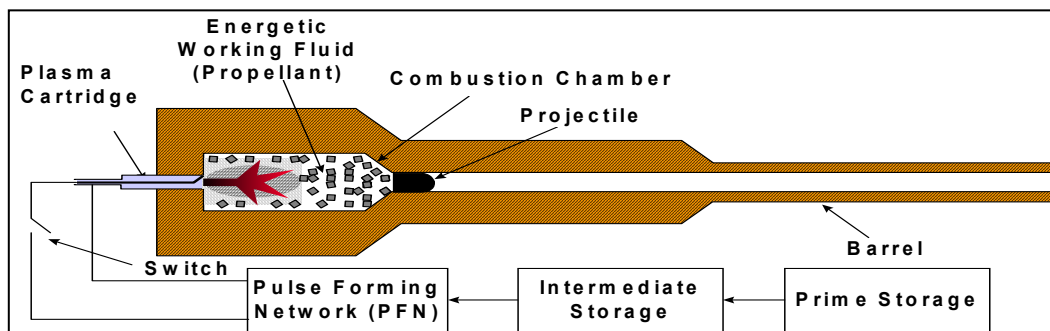


Figure 1. ETC gun concept.

Research has been carried out on a number of aspects of plasma and plasma/propellant interactions (5, 6). Because the plasma is at a temperature (typically  $>10,000$  K) that is considerably higher than conventional chemical igniters (3000 K), the radiation properties of the plasma have also been considered. The high plasma temperature leads to radiation effects nearly 100 times greater than that of chemical igniters (i.e., a  $T^4$  effect) (5). Such radiation could lead to significantly different temperature profiles within the propellant, causing changes in combustion rates. Another significant characteristic of the plasma is a much lower density than

the gases generated by a chemical igniter. The lower density plasma impacts the convective heat transfer to the propellant, as the plasma moves through the grains, as well as the velocity and mode of flamespreading within a propellant bed. It has been suggested that energy transport by convection may be as important as radiation transport in plasma-propellant interaction (PPI) (7, 8).

The effects previously described can lead to significant changes in ballistic behavior and useful improvements in gun performance once an understanding of the underlying physical mechanisms is achieved. To this end, the U.S. Army Research Laboratory (ARL) has begun a comprehensive study on the interaction of the plasma efflux from a ETC igniter with solid propellant grains. The goal of this work is to elucidate the relevant physical, mechanical, and chemical mechanisms that underlie the observed ballistic effects. Various aspects of the experimental program for PPI are described elsewhere (9). The first phase of the modeling effort in support of this PPI project involves a time-accurate computational fluid dynamics (CFD) code that has been written to include high-temperature thermodynamics, variable specific heats and transport properties (viscosity and thermal conductivity), and finite-rate (nonequilibrium) chemical kinetics (the mechanism is described in reference [10]). A separate capillary model described by McQuaid and Nusca (11, 12) supplies boundary conditions for the CFD code in terms of the physical and chemical properties of the plasma capillary efflux. Validation of the capillary model and the CFD code, including coupled chemistry, uses a series of experiments wherein a plasma jet is generated from a plasma cartridge; pressures in the resulting unsteady flowfield are measured using a probe.

---

## **2. Description of Open-Air Plasma Jet Experiment**

---

References (8) and (13) provide a full description of the experiment with a summary given herein. The general view of the plasma generator is shown in figure 2. The plasma capillary consists of standard polyethylene liner with dimensions of 102 mm in length and 6.35 mm in diameter. The nozzle consists of a circular tube of 2.9 cm in length and 1.3 cm in diameter that is directly adjacent to the end of the plasma capillary followed by another circular tube of 1.9 cm in length and 3.2 cm in diameter. As a result, the plasma efflux, generated by the capillary, is expanded through a step-configuration nozzle before emerging into the open air. A series of probes is positioned in the path of the plasma efflux; typically, a single-pressure probe is used (figure 2), but ongoing tests involve heat flux probes as well (13). To protect these probes, the plasma capillary is mounted behind a steel plate. The surface of this plate forms the upstream boundary for the numerical simulation, with a hole in the plate forming the inlet to the computational domain.

The pressure probe is placed 15 cm away from the surface of the plate and aligned with the centerline of the cartridge. The data acquisition system was chosen for maximum frequency response ( $>1$  MHz). The pressure gage was rated at 1.5 MHz and 0.2  $\mu$ s. Care was exercised

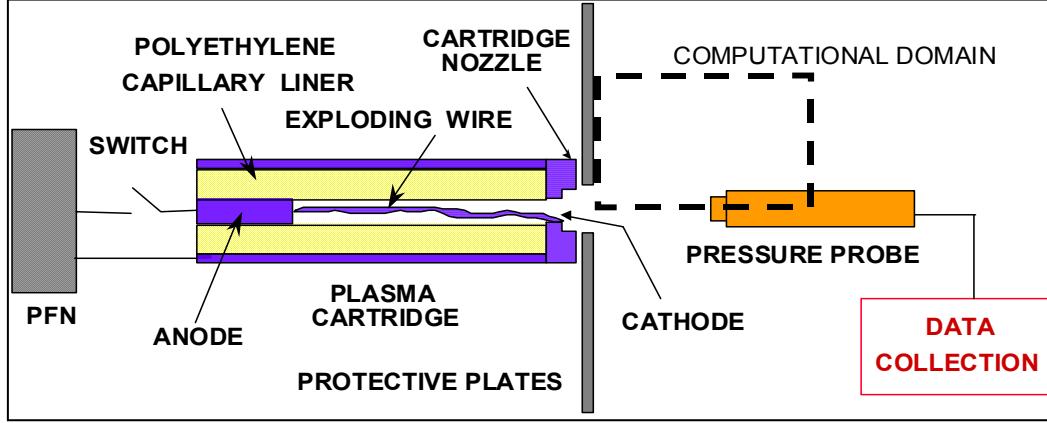


Figure 2. Schematic of plasma generator and pressure probe also showing computational domain.

in shielding the gage from direct interaction with the plasma as were the cables and amplifiers (strong evidence of charged particle impact on the unshielded gage was found [8]). Even so, post-firing examination of the pressure gage indicated significant amounts of particulate in the plasma effluent (the plasma is generated by ablation) that contributed to noticeable variability in pressure histories from shot to shot.

The electrical power supplied to the plasma generator used a five-stage, pulse-forming network (PFN) that could store up to 130 kJ (see reference [5]). The five stages could be charged to different voltages and fired at different times to obtain the desired power-pulse shape. The electrical data were recorded using a Rogowski coil for load current and a voltage divider and current transformer for load voltage. These data were used to generate load current, voltage, power, energy, and impedance as a function of time. Figure 3 shows the power and amplitude variation for a typical experiment. Given the amplitude/time and the physical characteristics of the capillary, the capillary model (11, 12) generates the range of density, velocity, pressure, temperature, and species distributions shown in figures 4–6.

Note that figure 3 shows a pulse forming network (PFN) pulse width of  $\sim 0.45$  ms, but figures 4–6 show efflux histories spanning  $\sim 0.275$  ms. The current/time data up to 0.027 ms and between 0.40 and 0.45 ms were ignored by the capillary model; the relatively small current levels during these times caused a divergence in the capillary model because a relatively small amount of plasma was being generated. As a result, the efflux histories were shifted to zero-time, and the CFD computation was started with efflux properties that characterized an abrupt rather than a more gradual start to the efflux; the computed time-of-arrival of the jet on the pressure probe will be shorter than measured (see section 5). A more amenable resolution to this problem is being formulated for future simulations. Figure 6 shows that there are five prominent species in the plasma efflux among a total of 31 species that were considered in the capillary model (11, 12) and 38 species in the CFD simulations (7 species were added for reaction with air). For a complete list of species, see table 1.

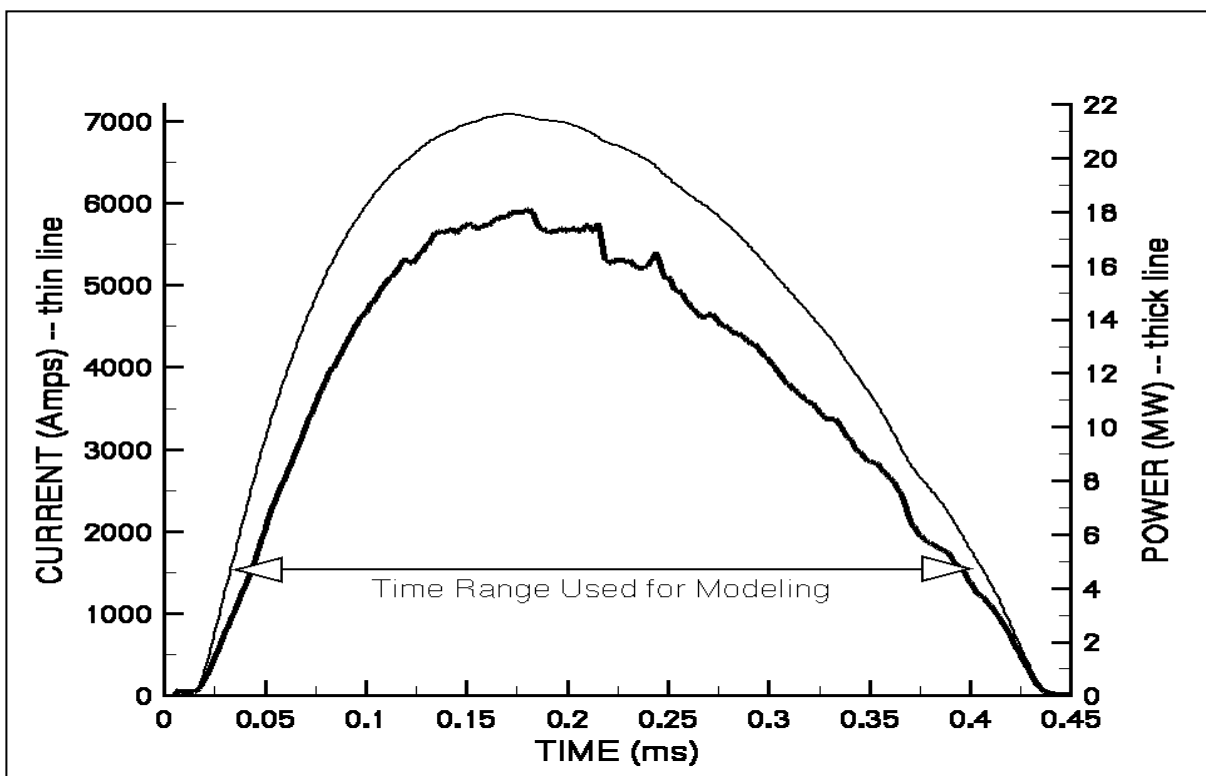


Figure 3. Current and power histories.

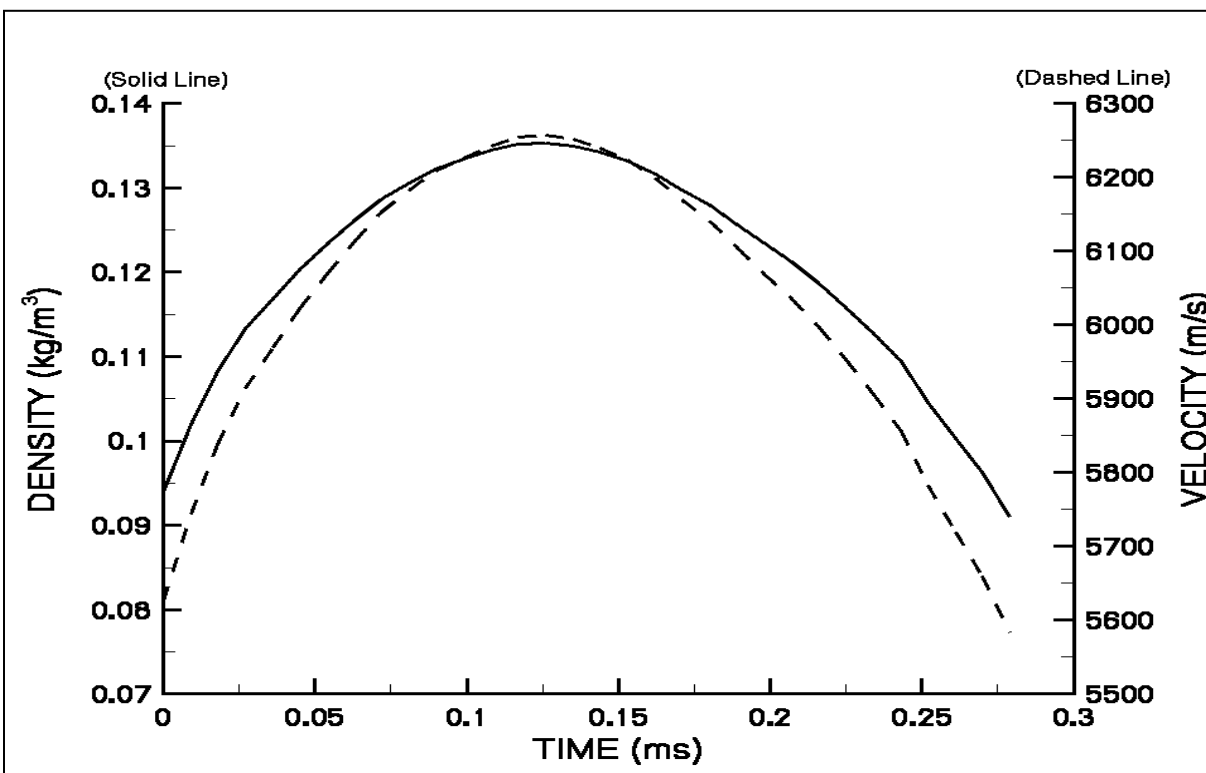


Figure 4. Efflux density and velocity histories.

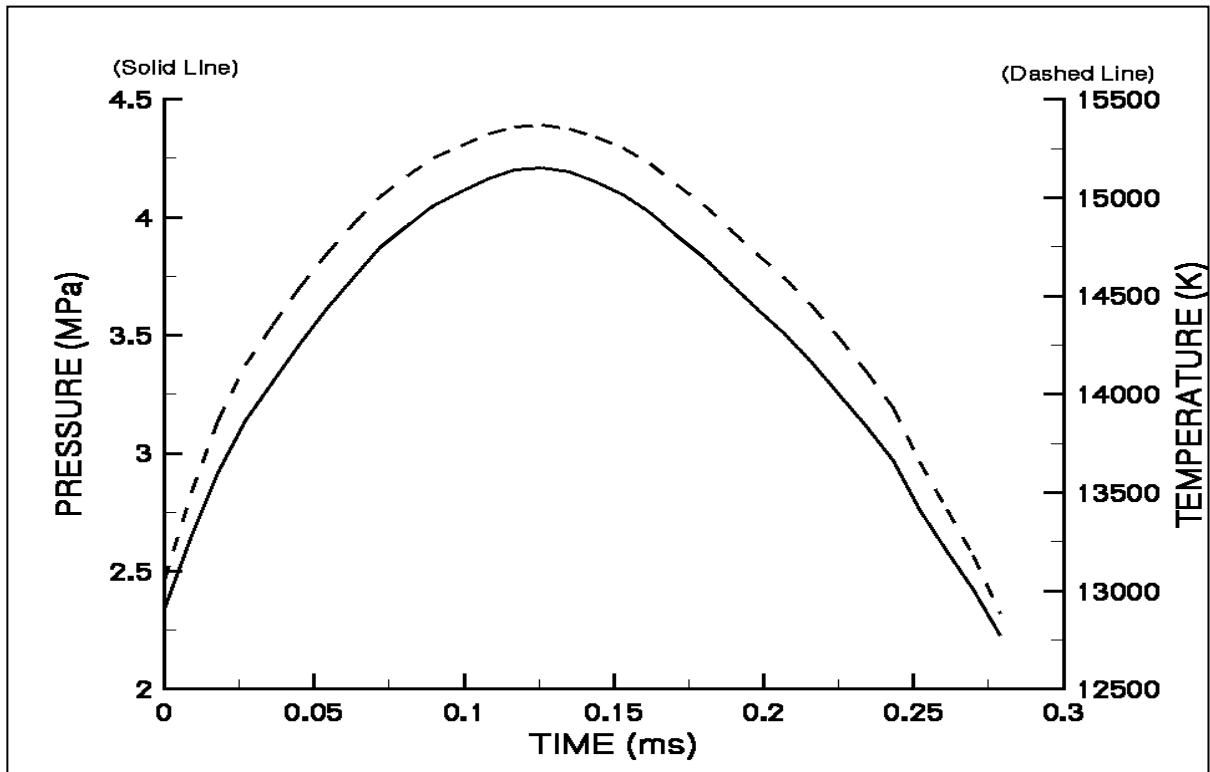


Figure 5. Efflux pressure and temperature histories.

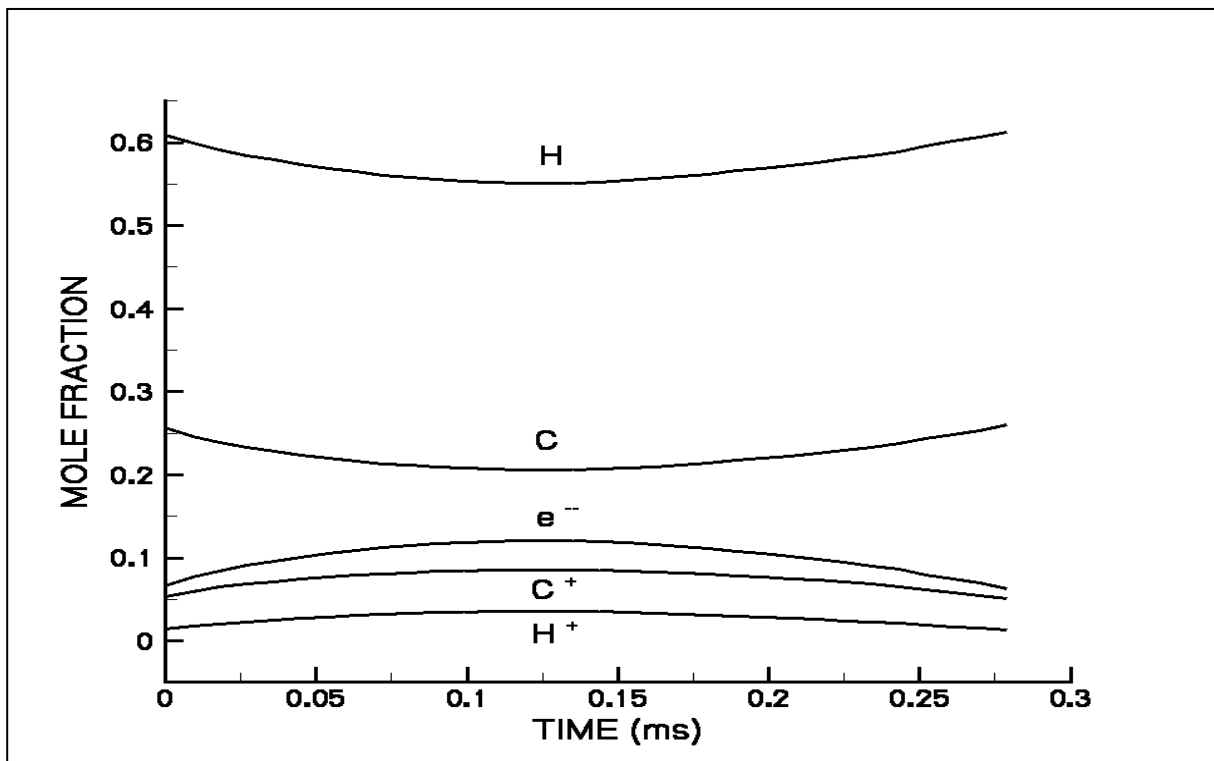


Figure 6. Efflux species histories.

Table 1. Species concentrations (moles/m<sup>3</sup>) at 0.22 ms and four locations along the centerline.

Species	Inlet	X = 1 cm	X = 9 cm	X = 15 cm (Probe Tip)
Electrons	0.0022	0.0026	0.0021	0.0435
C	0.0061	0.0048	0.0038	0 <sup>a</sup>
C+	0.0017	0.0019	0.0015	0.0327
C++	0 <sup>a</sup>	0 <sup>a</sup>	0 <sup>a</sup>	0 <sup>a</sup>
C-	1.07E-06	1.09E-06	8.53E-07	2.38E-07
CH	3.32E-06	2.38E-06	1.19E-06	6.66E-07
CH+	1.90E-06	1.99E-06	1.55E-06	4.27E-07
CN	9.48E-11	5.29E-11	4.32E-11	1.41E-11
CN+	9.16E-12	8.63E-12	6.79E-12	1.99E-12
CO	2.58E-10	3.41E-10	5.42E-10	0.0017
CO+	3.27E-11	2.59E-06	2.07E-06	0 <sup>a</sup>
C <sub>2</sub>	2.12E-06	1.27E-06	1.03E-06	4.05E-07
C <sub>2</sub> +	9.12E-07	8.16E-07	6.45E-07	1.95E-07
H	0.0152	0.0126	0.0099	0.0462
H+	5.40E-04	7.61E-04	5.80E-04	0.0429
H-	2.40E-06	2.78E-06	2.15E-06	5.57E-07
H <sub>2</sub>	4.28E-06	3.52E-06	2.82E-06	9.22E-05
H <sub>2</sub> +	5.43E-07	7.46E-07	5.71E-07	1.34E-07
N	9.25E-08	7.60E-08	6.03E-08	7.17E-08
N+	5.34E-09	7.62E-09	5.81E-09	1.33E-09
NH	4.98E-11	3.78E-11	3.02E-11	4.45E-12
NH+	1.14E-11	1.44E-11	1.11E-11	2.72E-12
NO	0 <sup>a</sup>	1.03E-16	5.80E-17	3.92E-12
NO+	3.31E-16	2.68E-11	2.14E-11	5.17E-08
N <sub>2</sub>	0 <sup>a</sup>	1.95E-18	3.82E-12	0.0061
O	1.33E-07	2.70E-06	2.15E-06	0.0767
O+	4.32E-09	6.24E-09	5.02E-09	0.0014
OH	6.80E-11	1.10E-10	1.09E-10	2.02E-04
OH+	1.33E-11	1.67E-11	1.28E-11	3.17E-12
O <sub>2</sub>	0 <sup>a</sup>	4.98E-16	6.26E-10	0 <sup>a</sup>
O <sub>2</sub> +	2.72E-17	8.96E-13	7.39E-10	0 <sup>a</sup>
H <sub>2</sub> O	0 <sup>a</sup>	1.08E-15	1.06E-15	1.46E-08
HO <sub>2</sub>	0 <sup>a</sup>	0 <sup>a</sup>	0 <sup>a</sup>	0 <sup>a</sup>
H <sub>2</sub> O <sub>2</sub>	0 <sup>a</sup>	0 <sup>a</sup>	0 <sup>a</sup>	0 <sup>a</sup>
HNO <sub>2</sub>	0 <sup>a</sup>	0 <sup>a</sup>	0 <sup>a</sup>	0 <sup>a</sup>
NO <sub>2</sub>	0 <sup>a</sup>	0 <sup>a</sup>	0 <sup>a</sup>	0 <sup>a</sup>
CO <sub>2</sub>	0 <sup>a</sup>	2.72E-21	1.21E-20	1.35E-08
O <sub>3</sub>	0 <sup>a</sup>	0 <sup>a</sup>	0 <sup>a</sup>	0 <sup>a</sup>
Density (mol/m <sup>3</sup> )	0.0274	0.0194	0.0153	0.0894
Pressure (atm)	31.7	21.1	22.7	62.8
Temp (K)	13950	13560	16770	8310

<sup>a</sup>Quantity is  $<1.0 \times 10^{-50}$ .

---

### 3. Previous Modeling Efforts

---

ARL, in cooperation with the Naval Research Laboratory (NRL), had conducted a computational study of open-air plasma discharges from 1997 to 1998 (14–16). This computational study was based on the NRL CFD code FAST3D (17) and sponsored by the Department of Defense Common High-Performance Computing Software Support Initiative program. The ARL open-air plasma firing was chosen as a test case for the FAST3D CFD code because the plasma jet is of a very high velocity and temperature, but of a very low density. The plasma jet was assumed to be an ideal neutral single-component gas with density, temperature, ratio of specific heats ( $\gamma$ ), and velocity characteristics identical to the plasma discharge. The multicomponent nature of the plasma, consisting of various neutral species, ions, electrons, and its chemical reactivity was not considered in those studies. The augmentation of plasma-air mixing, caused by viscosity and turbulence, was also excluded in these studies. The time-dependent gas properties, along with jet velocity and  $\gamma$ , were determined using a plasma capillary code developed at ARL by Powell and Zielinski (18). Overall, these CFD simulations captured the major features of the plasma jet as photographed by White et al. (5). Alternating bright-dark structures in the photos were identified as the shock structures in the jet. A precursor shock caused by the high-velocity/low-density plasma effluent (a feature not easily observed or photographed) was captured. Comparisons between computed and measured pressures in the jet were encouraging but pointed to the need for a variable  $\gamma$  multicomponent-reacting flow model.

---

### 4. Multispecies Reacting Flow CFD Code

---

The high-temperature, nonideal chemically reacting gas flowfield within the capillary efflux jet is numerically simulated using CFD. The NSRG2 code, written by Nusca (19–21), solves the two-dimensional (2-D)/axisymmetric, unsteady real-gas Navier-Stokes equations, including submodels that represent finite-rate (nonequilibrium) chemical reactions, multispecies diffusion, as well as variable specific heats, viscosity, and thermal conductivity. These partial differential equations are cast in conservation form and converted to algebraic equations using a finite-volume formulation. Solution takes place on a mesh of nodes distributed in a zonal fashion throughout the flowfield such that sharp geometric corners and other details are accurately represented. The conservation law form of the equations ensures that the end states of regions of discontinuity (e.g., shocks) are physically correct even when smeared over a few computational cells. The Navier-Stokes equations for 2-D/axisymmetric ( $x, y$  coordinates), reacting ( $N$  species), and unsteady (time,  $t$ ) flow are written in nondimensional form (19). The dependent variables are density ( $\rho$ ), velocity ( $V$  and components  $u, v$ ), energy ( $e$ ), and species mass fraction ( $c_i$ ). Pressure and temperature are  $p$  and  $T$ , whereas  $L$  is a characteristic lengthscale for the flowfield.

$$\frac{\partial U}{\partial t} + \frac{\partial F}{\partial x} + \frac{\partial G}{\partial y} + H = 0, \quad (1)$$

where

$$U = \left\{ \rho y^\alpha, \rho u y^\alpha, \rho v y^\alpha, \rho e y^\alpha, \rho c_1 y^\alpha, \dots, \rho c_N y^\alpha \right\},$$

$$F = \begin{Bmatrix} \rho u y^\alpha \\ (\rho u^2 + \sigma_{xx}) y^\alpha \\ (\rho u v + \tau_{xy}) y^\alpha \\ (\rho u e + u \sigma_{xx} + v \tau_{xy} + q_x) y^\alpha \\ (\rho u c_1 - \Lambda_1(c_1)_x - \Gamma_1(\ln T)_x) y^\alpha \\ \vdots \\ \vdots \\ \vdots \\ (\rho u c_N - \Lambda_N(c_N)_x - \Gamma_N(\ln T)_x) y^\alpha \end{Bmatrix}, \quad G = \begin{Bmatrix} \rho v y^\alpha \\ (\rho v u + \tau_{yx}) y^\alpha \\ (\rho v^2 + \sigma_{yy}) y^\alpha \\ (\rho v e + v \sigma_{yy} + u \tau_{xy} + q_y) y^\alpha \\ (\rho v c_1 - \Lambda_1(c_1)_y - \Gamma_1(\ln T)_y) y^\alpha \\ \vdots \\ \vdots \\ \vdots \\ (\rho v c_N - \Lambda_N(c_N)_y - \Gamma_N(\ln T)_y) y^\alpha \end{Bmatrix}, \quad H = \begin{Bmatrix} 0 \\ 0 \\ \alpha \sigma_+ \\ 0 \\ -\dot{w}_1 \\ \vdots \\ \vdots \\ \vdots \\ -\dot{w}_N \end{Bmatrix},$$

$$\sigma_{xx} = y^\alpha p + \frac{2\mu}{3y^\alpha Re} \left( \frac{\partial(y^\alpha u)}{\partial x} + \frac{\partial(y^\alpha v)}{\partial y} \right) - \frac{2\mu}{Re} \frac{\partial u}{\partial x}, \quad \Lambda = \frac{\mu Le}{Re Pr}, \quad \Gamma = k_T \Lambda, \quad Le = \frac{Pr}{Sc},$$

$$\sigma_{yy} = y^\alpha p + \frac{2\mu}{3y^\alpha Re} \left( \frac{\partial(y^\alpha u)}{\partial x} + \frac{\partial(y^\alpha v)}{\partial y} \right) - \frac{2\mu}{Re} \frac{\partial v}{\partial y}, \quad Sc = \frac{\mu}{\rho D}, \quad Re = \frac{\rho V L}{\mu}, \quad Pr = \frac{\mu c_p}{K},$$

$$\sigma_+ = p + \frac{2\mu}{3y^\alpha Re} \left( \frac{\partial(y^\alpha u)}{\partial x} + \frac{\partial(y^\alpha v)}{\partial y} \right) - \frac{2\mu}{Re} \frac{v}{y^\alpha}, \quad \Gamma_{xy} = \Gamma_{yx} = \frac{-\mu}{y^\alpha Re}, \quad = \left( \frac{\partial u}{\partial y} + \frac{\partial v}{\partial x} \right), \quad E = \frac{V^2}{h},$$

$$q_x = \frac{-K}{Re Pr E} \frac{\partial T}{\partial x} - \frac{\mu}{Re Pr} \sum_{i=1}^N Le h_i \frac{\partial c_i}{\partial x}, \quad \text{and} \quad q_y = \frac{-K}{Re Pr E} \frac{\partial T}{\partial y} - \frac{\mu}{Re Pr} \sum_{i=1}^N Le h_i \frac{\partial c_i}{\partial y}.$$

The diffusion coefficient,  $D$ , is understood to be the multicomponent coefficient,  $D_{im}$  (specie  $i$  into the mixture), which is related to the binary diffusion coefficient,  $D_{ij}$  (specie  $i$  diffusing into specie  $j$ ),

$$D_{ij} = \frac{1 - X_i}{\sum_j X_j / D_{ij}}, \quad D_{ij} = \frac{0.00266 T^{3/2}}{p M_{ij}^{1/2} \sigma_{ij}^2 \Omega_D}, \quad M_{ij} = \frac{2}{1/M_i + 1/M_j}, \quad (2)$$

where  $X_i$  is the mole fraction and  $M_i$  is the molecular weight of species  $i$ ,  $\Omega_D$  is the collision integral and  $\sigma_{ij}$  is the collision diameter (available in the literature). The thermal diffusion ratio,  $k_T$ , is assumed to be 1.0.

The relations for species enthalpy, mixture energy per unit volume, and pressure are given by the following state equations. It should be noted here that appropriate state equations for a



high-temperature plasma, which are somewhat more complex than these, are at the same time not widely available in the literature. The present choice of these relations will affect the results.

$$h_i = e_i + R_i T, \quad e = \frac{p}{\gamma - 1} + \frac{\rho(u^2 + v^2)}{2} + \sum_{i=1}^N \rho c_i \Delta H_{fi}^o, \quad p = \rho R T \sum_{i=1}^N \frac{c_i}{M_i}, \quad (3)$$

where  $\Delta H_i^o$  is the formation heat for species  $i$ . The ratio of specific heats is  $\gamma = c_p/c_v$ , where  $c_p$  and  $c_v$  are the mixture specific heats. The species values are computed using polynomials with coefficients  $\alpha_1$ – $\alpha_7$  (22). The specific gas constant is  $R_i$  (the universal constant is  $R$ ), and the heats can be related using  $C_{vi} = C_{pi} - R_i$ .

$$c_p = \sum_{i=1}^N c_{pi} c_i + \sum_{i=1}^N h_i \left( \frac{\partial c_i}{\partial T} \right)_p,$$

and

$$c_{pi} = R_i (a_1 T^{-2} + a_2 T^{-1} + a_3 + a_4 T + a_5 T^2 + a_6 T^3 + a_7 T^4). \quad (4)$$

Likewise, viscosity and thermal conductivity coefficients are given by polynomials with coefficients  $A$ ,  $B$ ,  $C$ , and  $D$  given in reference (22) (coefficients for each specie are different for each variable and each specie). The mixture values of viscosity and thermal conductivity are computed using empirical mixture rules discussed in reference (19).

$$\ln(\mu) = A_i \ln(T) + \frac{B_i}{T} + \frac{C_i}{T^2} + D_i, \quad \text{and} \quad \ln(\kappa) = A_i \ln(T) + \frac{B_i}{T} + \frac{C_i}{T^2} + D_i. \quad (5)$$

Chemical reactions can be expressed in a general reaction equation.  $X_i$  represents the symbol for specie  $i$ , and  $\nu$  is the stoichiometric coefficient for species  $i$  (primed for reactant and double-primed for product) in the reactions (10). The chemical source terms that appear in the  $H$  array for equation 1 (i.e.,  $w$ ) are computed using a general reaction rate equation. The reaction rates for each reaction,  $k$  (“f” for forward and “b” for backward), are usually expressed in Arrhenius form (see reference [19] for details) but often include corrections for high-pressure effects (see reference [10] for reaction rate data). The backward rate coefficients are computed from the forward values and the equilibrium constant for each reaction (19).

$$\sum_{i=1}^N \nu_i' X_i \xrightleftharpoons[k_b]{k_f} \sum_{i=1}^N \nu_i'' X_i, \quad \text{and} \quad \dot{w}_i = M_i (\nu_i'' - \nu_i') \left( k_f \prod_i C_i^{\nu_i'} - k_b \prod_i C_i^{\nu_i''} \right). \quad (6)$$

The Navier-Stokes equations (equation 1) are written in integral form and then re-expressed in a semi-discrete fashion using a finite-volume discretization technique. The numerical computations proceed by solving the semi-discrete equation on each computational cell using central and upwind numerical differences along with flux-limiting. Once properly discretized, the resulting set of algebraic equations is solved in a coupled manner in time, using an explicit time-accurate method. The numerical time-step is computed using the CFL condition. A separate chemical time-step is computed as well. The final time-step is based on the smallest of these. Nusca (19–21) offers a complete treatment of the numerical scheme.

---

## 5. Results and Discussion

---

The computational domain chosen to be used to simulate the experiment and sketched in figure 2 extends from the protective plate to a small distance along the pressure probe (0.18-m total length) and from the centerline of the capillary (and probe) to a small radial distance (0.08-m total radius). This region was discretized using 277 axial grid cells and 160 radial grid cells, distributed in essentially an even spacing throughout. The boundary conditions for this region are symmetry on the axis ( $Y = 0$ ), outflow at  $X = 0.18$  m and  $Y = 0.08$  m, no-slip/no-penetration on the plate surface ( $X = 0$ ,  $0.0159 < Y < 0.08$  m) and the probe surface, and specified inflow at the capillary exit ( $X = 0$ ,  $0 < Y < 0.0159$  m). The inflow conditions follow from those displayed in figures 4–6 (note: see table 1 for a complete list of species specified at the inlet). Initially, the entire flowfield is filled with air (0.8 mole fraction of  $N_2$  and 0.2 mole fraction of  $O_2$ ).

To aid in the interpretation of computational results for the plasma jet, figure 7 shows a schematic of the expected gas dynamic features as have been observed in highly underexpanded supersonic jets (23, 24). The efflux of plasma from the inlet generates a weak precursor shock (A) that expands spherically. Behind this shock is air; the plasma is entirely contained by this shock and is separated from the air by an irregularly shaped contact surface (B) across which pressure and velocity are preserved, but entropy changes discontinuously. Expansion waves (C), generated at the inlet, travel to the precursor shock (A), are reflected as weak compression waves, and coalesce into a strong oblique shock or barrel shock (D) within the plasma jet. This barrel shock (D) terminates in an irregular reflection that forms a triple-point (E), joining the barrel shock (D), its reflection (F), and a normal shock (G) or Mach disk. Whereas the precursor shock (A) is relatively weak and diffuse, producing a mildly supersonic flow, the barrel shock (D) and Mach disk (G) are strong shocks that enclose a fully supersonic flow region.

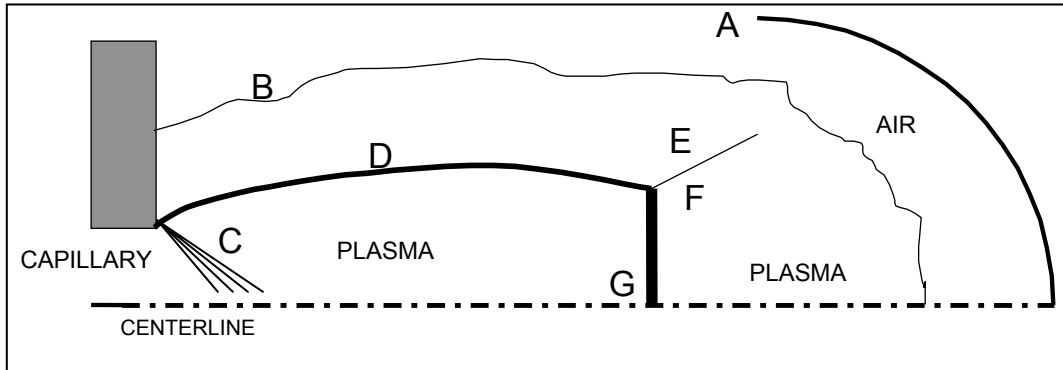


Figure 7. Schematic of gas dynamic features in a highly underexpanded jet.

Figure 8 shows the time history of the plasma jet from shortly after entrance into open-air (0.05 ms) to shortly after impact upon the pressure probe (0.24 ms). Note that the frames in figure 8 are not evenly spaced in time but are chosen to highlight the features of figure 7. Mach number contours are displayed in gray-scale from 0 (bright white) to 1.6 and above (dark black). As the low-density ( $0.08\text{-kg/m}^3$ ) plasma efflux enters the open-air, a precursor shock is formed. At this time, the jet is moving at  $\sim 5600\text{ m/s}$ , which is  $\sim \text{Mach } 1.6$ , based on the local sound speed in the mixture (note that the plasma gas is of very low molecular weight,  $\sim 4.3$ ). By  $\sim 0.20\text{ ms}$ , the predominant gas dynamic features in the jet have been established, including the intersection of the barrel shock with the Mach disk ( $X = 0.06\text{ m}$ ) and a weak reflected shock. Due to the variable viscosity in the flowfield (see equation 5), the precursor shock is more diffuse than the normal shock of the Mach disk or the oblique “barrel” shock. Note the subsonic flow region between the normal shock and the precursor shock; within this region resides the contact surface. The precursor shock reaches the pressure probe at  $\sim 0.22\text{ ms}$ . Stagnation of supersonic flow on the probe tip causes a normal shock to standoff from the probe. By  $0.24\text{ ms}$ , this tip shock is no longer required because the flow is subsonic in the probe’s near field. Figure 9 shows the measured and computed pressure at the probe tip. As was discussed in relation to figure 3, the computed pressure history has been shifted by  $0.027\text{ ms}$ . Even so, the computed precursor shock arrives at the probe  $\sim 0.02\text{ ms}$  early and registers a pressure that is  $\sim 30\%$  higher than measured. Computed pressure oscillations around the peak are due to the unsteady nature of the normal shock at the probe tip. The presence of particulates in the flow stream reported by White et al. (8) may account for some of this discrepancy as may the absence of both a true plasma equation of state (see equation 3) and radiation energy losses in the computations. At this point in time, the computation was halted until further investigations of the source of the pressure overprediction was discovered.

Figures 10 and 11 show computed results for the plasma jet at  $0.13\text{ ms}$  and  $0.22\text{ ms}$ , respectively, in terms of eight variables. The pressure and temperature have been normalized by one atmosphere and  $300\text{ K}$ , the values ahead of the precursor shock, respectively. The heat capacity ( $c_p$ ), thermal conductivity ( $\kappa$ ), and viscosity ( $\mu$ ) have been nondimensionalized using the values for air; therefore, ahead of the precursor shock, these variables are 1.0. At  $0.13\text{ ms}$  (figure 10), the precursor shock is indicated by the sharp pressure gradient at  $X = 0.09\text{ m}$  from the inlet (the spherical shape of this shock is distorted by the plotting scale). The normal shock (Mach disk) at  $X = 0.035\text{ m}$  is clearly visible in the pressure contour map, as is the high-pressure flow from the inlet. Behind the precursor shock and in front of the normal shock (i.e.,  $0.035 < X < 0.09\text{ m}$ ), the pressure and temperature are quite high, indicating extreme compression of the flow due to these two shocks. The plots of heat capacity and thermal conductivity highlight the region of plasma (note the piston-like shape with expanded leading edge) in which these variables take on values that are much higher than those in ambient air. The plot of viscosity indicates that the plasma

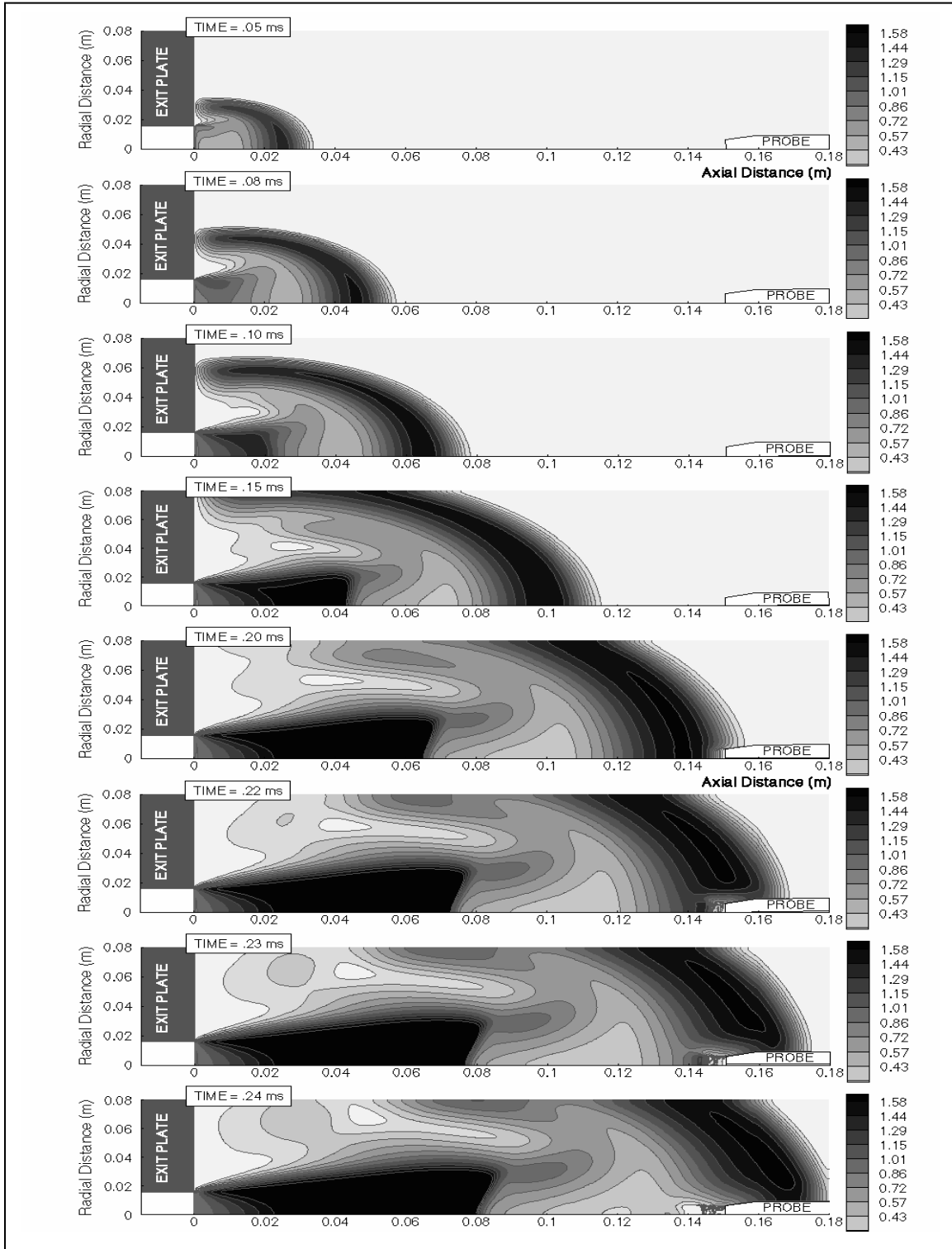


Figure 8. Computed Mach number contours.

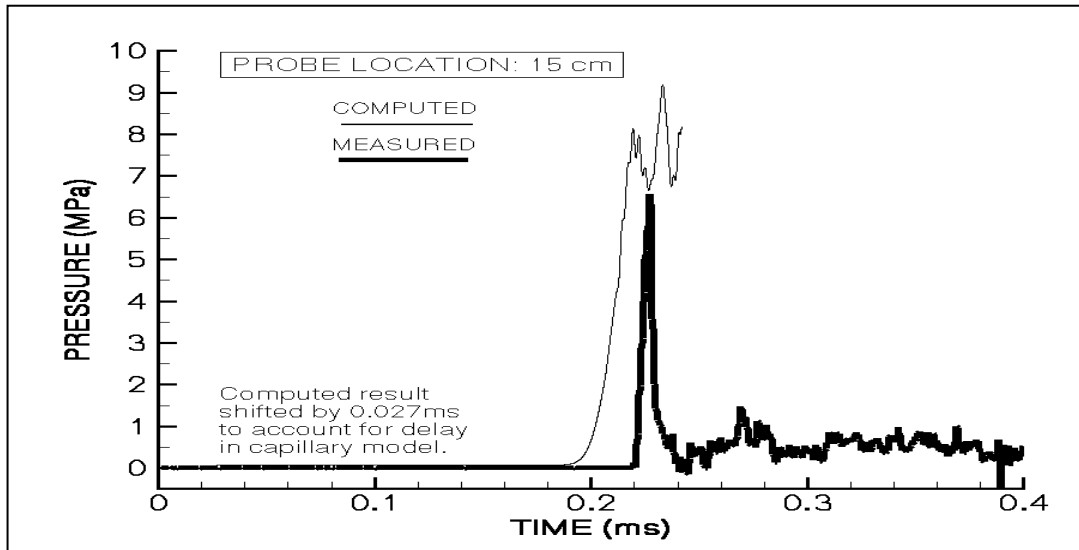


Figure 9. Measured and computed pressure at the probe tip.

itself represents largely laminar flow (i.e., high value of viscosity). The plot of hydrogen (H) atom concentration confirms that the plasma consists mainly of H gas (figure 6) and electrons (the plot of electron concentration is qualitatively similar to the plot of H). In the high-pressure and high-temperature region, the density is also high and causes the largest local concentration of H away from the inlet. The formation of OH and CO<sub>2</sub> will not take place until sufficient thermal and chemical conditions arise in the flowfield, as dictated by the detailed chemical kinetics mechanism (the reader is referred to reference [10]). The contour plots of these species indicate that such conditions do exist outside the plasma core region ( $0 < X < 0.055$  m,  $0 < Y < 0.018$  m at this time) where mixing with air (i.e., O<sub>2</sub> and N<sub>2</sub>) is sufficient. Space limitations do not permit the displaying of all chemical species distributions, but this information is being probed as a means of characterizing the chemical nature of the plasma efflux. Figure 11 shows the same variables plotted for 0.22 ms in time, when the leading edge of the plasma jet (i.e., the precursor) has just reached the probe. Flow stagnation on the probe tip causes local compression, and a bow shock is generated on the tip (see pressure plot). Gas temperature (and density) also increases near the probe as does the concentration of H. Flow heating, species mixing with air, and chemical reactions cause increased concentrations of OH (especially) and CO<sub>2</sub>; this indicates increased levels of chemical reaction in the flowfield. Of course, the probe's near-field properties continually change as subsequent regions of the jet flow impinge upon the tip (i.e., after the precursor shock, the contact surface, and the Mach disk containing a region of supersonic flow).

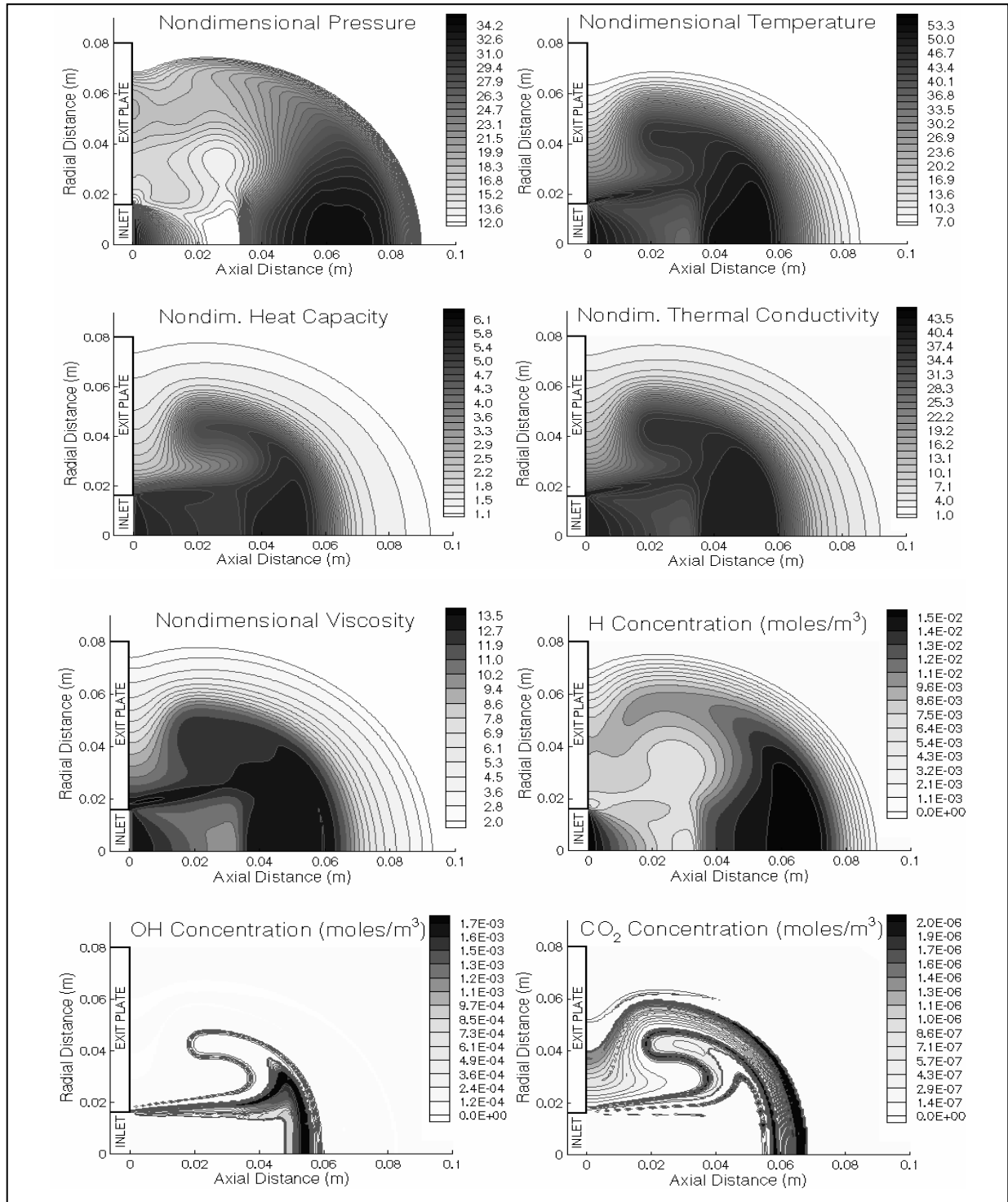


Figure 10. Computational results displayed in eight contour variables for 0.13 ms.

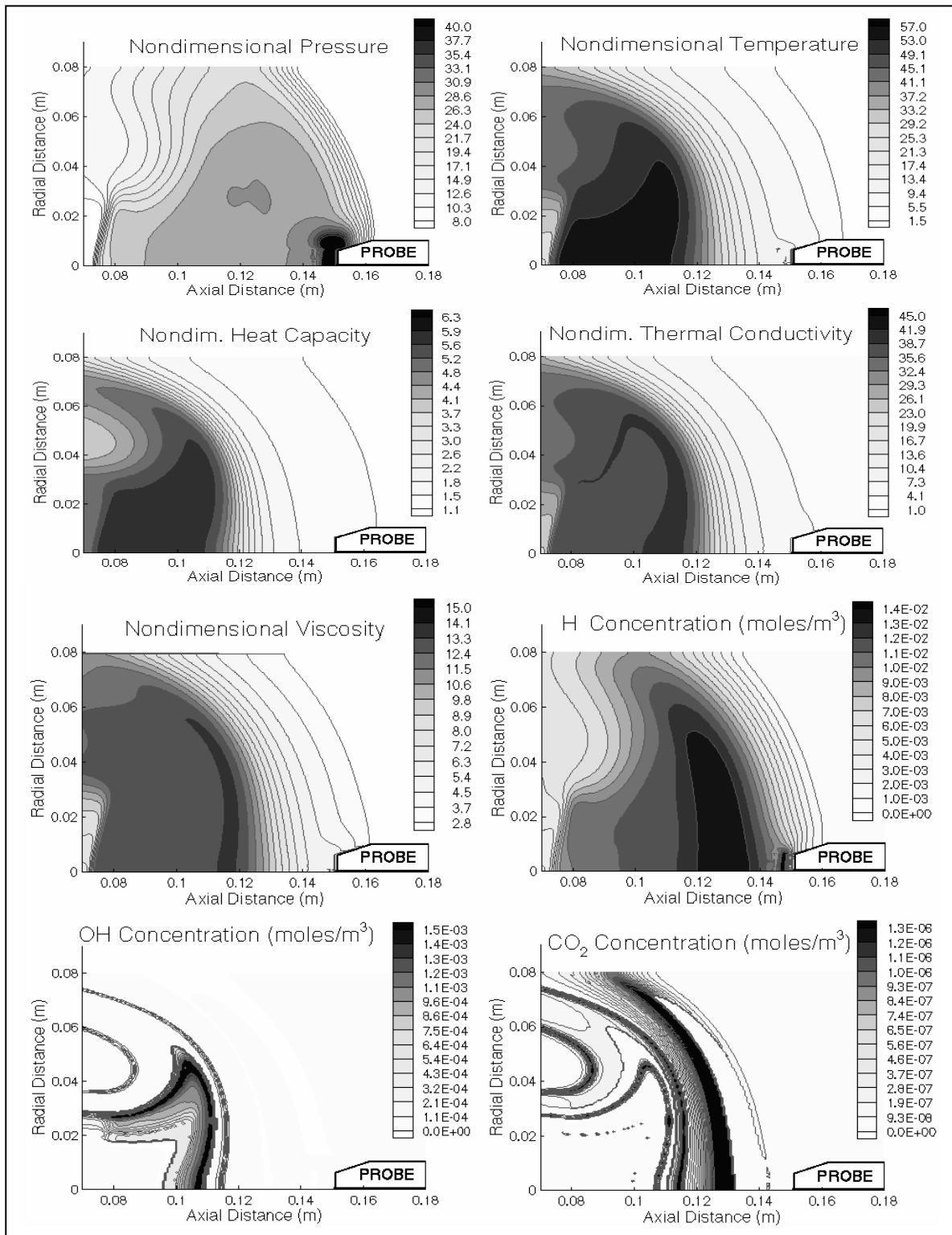


Figure 11. Computational results displayed in eight contour variables for 0.22 ms.

After looking at these results, one can suppose that the physical and chemical nature of the plasma efflux in the vicinity of the probe is very different from that near the capillary. Gas dynamic expansion in open air has caused the generation of various shocks and mixing layers that have combined the plasma species with air and have resulted in chemical reactions. Table 1 lists the species considered in the present model and provides the concentrations for a time of 0.22 ms (i.e., displayed in figure 11) and at three locations along the centerline of the jet: at the inlet (i.e., capillary exit plane), just outside of the inlet, just ahead of the Mach disk, and within the precursor shock at the stagnation region on the probe tip. It is interesting to note the increased concentrations of various species at the probe tip, especially those species that are not predominant at the capillary ( $\text{CO}$ ,  $\text{NO}^+$ ,  $\text{N}_2$ ,  $\text{O}$ ,  $\text{O}^+$ ,  $\text{OH}$ ,  $\text{H}_2\text{O}$ ,  $\text{CO}_2$ ), and those abundant in the plasma that have collected on the tip ( $\text{H}$ ,  $\text{H}^+$ ,  $\text{C}^+$ , electrons). The C atom, abundant in the plasma efflux at the capillary, is absent at the probe tip (possibly combined in  $\text{CO}$  and  $\text{CO}_2$ ). These results confirm the supposition. The ultimate goal is to understand how the propellant responds to the plasma jet both mechanically (i.e., pressure and thermal loading from the shock system) and chemically. This information concerning the pressure, temperature, and chemical conditions at the probe tip are necessary starting conditions for subsequent modeling of solid propellant combustion in the plasma stream.

---

## 6. Conclusions

---

A time-accurate CFD code has been applied to the modeling of the high-temperature, chemically reactive plasma efflux from an ETC igniter fired into open air. The CFD code has been linked to a plasma capillary model for purposes of specification of the exit conditions of the igniter. The major features of this efflux have been resolved by numerical simulation revealing a highly underexpanded jet with a strong precursor shock, a barrel shock that reflects at a triple-point, and a normal shock or Mach disk. Impact of the jet upon a probe generates an intermittent bow shock on the probe tip that is dissipated in the low-velocity flow ahead of the Mach disk and is then re-established with the passage of this normal shock. The presence of this shock system has important implications for mechanical damage to solid propellant exposed to the plasma efflux. Chemical conditions at the probe are quite different from those at the ETC igniter. These computer simulations represent the first such detailed modeling of ETC igniter plasma efflux.



---

## 7. References

---

1. Del Güercio, M. Propellant Burn Rate Modification by Plasma Injection. *Proceedings of the 34th JANNAF Combustion Subcommittee Meeting*, West Palm Beach, FL, 1997; CPIA Publication 662, Vol. 1, 35–42.
2. Perelmutter, L.; Sudai, M.; Goldenberg, C.; Kimhe, D.; Zeevi, Z.; Arie, S.; Melnik, M.; Melnik, D. Temperature Compensation by Controlled Ignition Power in SPETC Guns, *Proceedings of the 16th International Symposium on Ballistics*, San Francisco, CA, 1996; NDIA, Vol. 1, 145–152.
3. Dyvik, J. A.; Katulka, G. L. ETC Temperature Compensation; Experimental Results of 120-mm Test Firings, *Proceedings of the 33rd JANNAF Combustion Subcommittee Meeting*, Monterey, CA, 1996; CPIA Publication 653, Vol. 3, 111–119.
4. Katulka, G. L.; Dyvik, A. Experimental Results of Electrical Plasma Ignition in 120-mm Solid Propellant Tank Gun Firings, *Proceedings of the 33rd JANNAF Combustion Subcommittee Meeting*, Monterey, CA, 1996; CPIA Publication 653, Vol. 3, 103–110.
5. White, K. J.; Katulka, G. L.; Khuan, T.; Nekula, K. *Plasma Characterization for Electrothermal-Chemical (ETC) Gun Applications*; ARL-TR-1491; U.S. Army Research Laboratory: Aberdeen Proving Ground, MD, September 1997.
6. Perelmutter, L.; Goldenberg, C.; Sudai, M.; Alimi, R.; Furman, M.; Kimhe, D.; Appelbaum, G.; Arie, S.; Zeevi, Z.; Melnik, D. Experimental Study of Plasma Propagation and Ignition of Solid Propellant in a Gun Chamber, *Proceedings of the 16th International Symposium on Ballistics*, San Francisco, CA, September 1996.
7. Nusca, M. J.; White, K. J. Plasma Radiative and Convective Interactions With Propellant Beds, *Proceedings of the 34th JANNAF Combustion Subcommittee Meeting*, West Palm Beach, FL, 1997; CPIA Publication 662, Vol. 1, 21–42.
8. White, K. J.; Williams, A. W.; Nusca, M. J. Plasma Output and Propellant Radiation Absorption Characteristics, *Proceedings of the 35th JANNAF Combustion Subcommittee Meeting*, Tuscon, AZ, 1998; CPIA Publication 680, Vol. 1, 237–246.
9. Kaste, P. J.; Birk, A.; Del Güercio, M. A.; Lieb, R.; Kinkennon, A. Surface Phenomena of Plasma-Treated Propellant Samples, *Proceedings of the 36th JANNAF Combustion Subcommittee Meeting*, Cocoa Beach, FL, 1999; CPIA Publication 691, Vol. 2, 77–98.
10. Anderson, W. R.; Schroeder, M. A. Chemical Mechanism for ETC Plasma Interaction With Air, *Proceedings of the 36th JANNAF Combustion Subcommittee Meeting*, Cocoa Beach, FL, 1999; CPIA Publication 691, Vol. 2, 43–54.

11. McQuaid, M. J.; Nusca, M. J. Calculating the Chemical Compositions of Plasmas Generated by an Ablating-Capillary Arc Ignition System, *Proceedings of the 36th JANNAF Combustion Subcommittee Meeting*, Cocoa Beach, FL, 1999; CPIA Publication 691.
12. McQuaid, M. J.; Nusca, M. J. *Calculating the Chemical Compositions of Plasmas Generated by an Ablating-Capillary Arc Ignition System*; ARL-TR-2046; U.S. Army Research Laboratory: Aberdeen Proving Ground, MD, 1999.
13. Williams, A. W.; White, J. Plasma-Propellant Interaction Studies: Measurements of In-Depth Propellant Heating by Plasma Radiation; Investigation of Possible Plasma-Induced Propellant Erosion, *Proceedings of the 36th JANNAF Combustion Subcommittee Meeting*, Cocoa Beach, FL, 1999; CPIA Publication 691, Vol. 2, 67–76.
14. Nusca, M. J.; White, K. J.; Young, T. R.; Landsberg, A. M. Computational Simulation and Experimental Visualization of an Open-Air Plasma Discharge, *Proceedings of the 34th JANNAF Combustion Subcommittee Meeting*, West Palm Beach, FL, 1997; CPIA Publication 662, Vol. 1, 43–56.
15. Nusca, M. J.; White, K. J.; Landsberg, A. M.; Lind, C. A.; Young, T. R. Computational Simulations of ETC Igniters and Plasma Discharge Experiments, *Proceedings of the 35th JANNAF Combustion Subcommittee Meeting*, Tuscon, AZ, 1998; CPIA Publication 680, Vol. 1, 219–227.
16. Nusca, M. J.; White, K. J.; Williams, A. W.; Landsberg, A. M.; Young, T. R.; Lind, C. A. Computational and Experimental Investigations of Open-Air Plasma Discharges, *37th AIAA Aerospace Sciences Meeting*, Reno, NV, January 1999; AIAA Paper 99-0865.
17. Boris, J. P.; Landsberg, A. M.; Oran, E. S.; Gardner, J. H. *LCPFCT – A Flux-Corrected Transport Algorithm for Solving Generalized Continuity Equations*; NRL MR 93-7192; Naval Research Laboratory: Washington, DC, 1993.
18. Powell, J.; Zielinski, A. *Theory and Experiment for an Ablating-Capillary Discharge and Application to Electrothermal Chemical Guns*; BRL-TR-3355; U.S. Army Ballistic Research Laboratory: Aberdeen Proving Ground, MD, June 1992.
19. Nusca, M. J. Numerical Simulation of Electromagnetic Wave Attenuation in Nonequilibrium Chemically Reacting Flows. *Computers and Fluids* **1998**, 27 (2), 217–238.
20. Nusca, M. J. Numerical Simulation of the Ram Accelerator Using a New Chemical Kinetics Mechanism. *Journal of Propulsion and Power* **2002**, 18 (1), 44–52.
21. Nusca, M. J.; Dinavahi, S. P. G.; Soni, B. Grid Adaptation Studies for Reactive Flow Modeling of Propulsion Systems, *American Institute of Aeronautics and Astronautics, 37th AIAA Aerospace Sciences Meeting*, Reno, NV, January 1999; AIAA Paper 99-0970.

22. McBride, B. J.; Gordon, S. *Computer Program for Calculation of Complex Chemical Equilibrium Compositions and Applications II. Users Manual and Program Description*; NASA RP 1311; NASA: Cincinnati, OH, June 1996.
23. Wilson, D. E.; Raja, L. L.; Petviashvili, N. Theoretical Analysis of the External Pulsed Propellant and Plasma Jets, *American Institute of Aeronautics and Astronautics, 36th AIAA Aerospace Sciences Meeting*, Reno, NV, January 1998; AIAA Paper 98-1000.
24. Schmidt, E. M.; Shear, D. D. Optical Measurements of Muzzle Blast. *AIAA Journal* **1975**, *13* (8), 1086–1091.

<u>NO. OF COPIES</u>	<u>ORGANIZATION</u>	<u>NO. OF COPIES</u>	<u>ORGANIZATION</u>
1 (PDF Only)	DEFENSE TECHNICAL INFORMATION CTR DTIC OCA 8725 JOHN J KINGMAN RD STE 0944 FT BELVOIR VA 22060-6218		<u>ABERDEEN PROVING GROUND</u>
1	COMMANDING GENERAL US ARMY MATERIEL CMD AMCRDA TF 5001 EISENHOWER AVE ALEXANDRIA VA 22333-0001	1	DIR USARL AMSRD ARL CI OK TP (BLDG 4600)
1	INST FOR ADVNCD TCHNLGY THE UNIV OF TEXAS AT AUSTIN 3925 W BRAKER LN STE 400 AUSTIN TX 78759-5316		
1	US MILITARY ACADEMY MATH SCI CTR EXCELLENCE MADN MATH THAYER HALL WEST POINT NY 10996-1786		
1	DIRECTOR US ARMY RESEARCH LAB AMSRD ARL CS IS R 2800 POWDER MILL RD ADELPHI MD 20783-1197		
3	DIRECTOR US ARMY RESEARCH LAB AMSRD ARL CI OK TL 2800 POWDER MILL RD ADELPHI MD 20783-1197		
3	DIRECTOR US ARMY RESEARCH LAB AMSRD ARL CS IS T 2800 POWDER MILL RD ADELPHI MD 20783-1197		

<u>NO. OF COPIES</u>	<u>ORGANIZATION</u>
	<u>ABERDEEN PROVING GROUND</u>
30	DIR USARL AMSRD ARL WM BD W ANDERSON R BEYER A BRANT S BUNTE L CHANG T COFFEE J COLBURN P CONROY G COOPER B FORCH A HORST S HOWARD S KARNA P KASTE A KOTLAR M MCQUAID A MIZIOLEK J NEWILL M NUSCA (6 CPS) R PESCE-RODRIQUEZ P PLOSTINS J SAHU S SILTON P WEINACHT A WILLIAMS

INTENTIONALLY LEFT BLANK.